SOFT ROBOTICS
Volume 00, Number 00, 2022

DOI: 10.1089/soro.2021.0116

SoRo
Soft Robotics

Open camera or QR reader and scan code to access this article and other resources online.

Fluid-Driven Traveling Waves in Soft Robots

Lior Salem,[i] Amir D. Gat, and Yizhar Or[ii]

Abstract

Many marine creatures, gastropods, and earthworms generate continuous traveling waves in their bodies for locomotion within marine environments, complex surfaces, and inside narrow gaps. In this work, we study theoretically and experimentally the use of embedded pneumatic networks as a mechanism to mimic nature and generate bidirectional traveling waves in soft robots. We apply long-wave approximation to theoretically calculate the required distribution of pneumatic network and inlet pressure oscillations needed to create desired moving wave patterns. We then fabricate soft robots with internal pneumatic network geometry based on these analytical results. The experimental results agree well with our model and demonstrate the propagation of moving waves in soft robots, along with locomotion capabilities. The presented results allow fabricating soft robots capable of continuous moving waves using the common approach of embedded pneumatic networks and requiring only two input controls.

Keywords: soft robotics, traveling waves, wavelike robot, under-actuated soft robots, fluid–structure interaction

Introduction

Many invertebrate creatures, such as gastropods, cuttlefish, and flagellated microorganisms, generate traveling waves in their bodies for locomotion, exploiting their flexibility to move in various unpredictable environments. Soft-robots, which have the ability to deform their flexible geometry, are inspired by these natural organisms and aim to mimic their capabilities.[1–3] Consequently, soft robots have diverse techniques for locomotion that suit their surroundings, such as legged locomotion,[4–7] crawling,[8–10] rolling,[11,12] swimming,[13–17] and so on.

Previous studies examined, both theoretically and experimentally, various approaches for the actuation of traveling waves for locomotion of soft robots.[18–21] Among the suggested methods are electroactive actuation[22–24] and surface wave robots.[25–27] Yet, the most commonly used approach to actuate soft robots is by pressurizing embedded fluidic channels, creating large amplitude waves.

Multiple inlets may actuate such robots, where each elastic segment is controlled separately to create a wave-like motion.[28–30] However, reducing the number of inlets may result in a more simple structure containing less hardware such as tubes, valves, and controllers. This approach may be applicable in confined spaces and in cases where lightweight and minimal implementation is crucial, such as in space missions.[31]

To realize a reduced number of controlled inlets for creating traveling wave motion, several works presented designs that consist of three inflated chambers which actuated

Faculty of Mechanical Engineering, TSAP - Technion Autonomous Systems and Robotics Program, Technion - Israel Institute of Technology, Technion City, Israel.
[i]ORCID ID (https://orcid.org/0000-0003-1415-3086).
[ii]ORCID ID (https://orcid.org/0000-0002-9091-9357).

sequentially with a phase difference. By transferring between three different geometries, the authors were able to create semicontinuous and approximate traveling wave motion in soft robots. More specifically, Takayama *et al.*[32] presented a soft robot composed of three bonded and twisted inlet tubes. The inlet pressure was alternating between the different tubes to generate helical rotation, which was utilized for locomotion through a pipe. Ozaki *et al.*[33] developed a three-chamber actuator that was wrapped around an endoscope and actuated sequentially to create traveling waves on the surface which exploited for self-propulsion.

A design of a soft robot which generates transverse waves, presented by Watanabe and Tsukagoshi,[34] consists of a sophisticated arrangement of three internal rubber tubes, limited-strain sleeve, and fabric layers that restrain radial and axial expansion. Similar to previous cases, the three tubes are pressurized sequentially, generating transverse traveling wave motion and crawl on the surface. Another relevant work by Qi *et al.*[35] exhibited a three-dimensional (3D) printed modular robot, designed using finite element software, that uses four types of similar modules that differ only by their internal air pathways. Thus, modules can be assembled serially and controlled by four inlets to form approximated traveling wave motion regardless of the number of modules. Moreover, several studies leveraged viscosity and fluid dynamics to minimize the number of controlled inlets for generating propulsion.[36–39]

The current work aims to demonstrate the use of an embedded pneumatic network, a common actuation method in soft robots, to mimic nature and generate continuous bi-directional traveling waves while using only two inlets. To achieve this, we derive a theoretical model and apply standard and simple fabrication techniques to experimentally demonstrate this approach. We then analyze the generated waves to calibrate the inlets and compare our analytic and experimental results. The main contributions of this work are: (i) Model-based formation of continuous traveling waves in fluid-actuated elastic structure using only two pressure inlets. (ii) Fabrication, identification, and calibration of fluid-driven traveling waves in elastic structure. (iii) Kinematic analysis and demonstration of the crawling locomotion of traveling wave robot on the rigid surface under no-slip kinematic constraint.

Analysis: Traveling Waves Based on Two Pneumatic Network

Spatially distributed fluid channels embedded in the elastic body in addition to time-dependent pressure inlets are combined to create traveling wave motion. This model-based design reduces the number of inlets to two. This section presents the derivation of the design concept.

We model the robot as a rectangular cross-section elastic beam with height h, width w, and length l, with embedded parallel channel network. The calculation of the beam's deformation induced by pressure can be realized from the modified Euler–Bernoulli equation as reported in previous works,[40–42]

$$\frac{\partial^2}{\partial x^2}\left[EI\left(\frac{\partial^2 y}{\partial x^2}+\phi(x)p(x,t)\frac{1}{E}\frac{\partial \psi}{\partial (p/E)}\right)\right]+c\frac{\partial y}{\partial t}+\rho_s A_s\frac{\partial^2 y}{\partial t^2}=q, \tag{1}$$

where x is an actuator-spatial longitudinal coordinate, $y=y(x,t)$ is lateral deformation, E is Young's modulus, I is second moment of the beam cross-section, $\phi(x)$ is channel density distribution (number of channels per unit length), $p(x,t)$ is fluid pressure in channels, $\partial\psi/\partial(p/E)$ is beam slope change due to a single channel at pressure p, c is structural damping, ρ_s is solid density, A_s is cross-section area, and $q(x,t)$ is distributed external load (Fig. 1).

To create the desired deformation pattern, our design aims to calculate the channel distribution, which is combination of two indexed channels, $\phi_1(x)$, $\phi_2(x)$, and corresponding time-dependent pressure inlets $p_1(t), p_2(t)$. Applying Equation (1), with the assumption of negligible inertia and viscosity and no external loads yields a relation between deformation and two sets of channels and inputs,

$$-\frac{\partial^2 y}{\partial x^2}=\frac{\partial \psi}{\partial (p/E)}(\phi_1(x)p_1(t)+\phi_2(x)p_2(t)). \tag{2}$$

Note that the solid's inertial effects are assumed to be negligible when the actuation frequencies are relatively slower than the dynamic natural frequencies. In such case, the structure moves along static equilibrium states. The desired deformation pattern of a single wavelength and a single frequency traveling wave is described as,

$$y(x,t)=A\cos\left(\omega t-\frac{2\pi x}{\lambda}\right), \tag{3}$$

where A is the wave amplitude, ω is its frequency, and λ is the spatial wavelength. Another equivalent form to represent this traveling wave is

$$y(x,t)=A\left(\cos\left(\frac{2\pi x}{\lambda}\right)\cos(\omega t)+\sin\left(\frac{2\pi x}{\lambda}\right)\sin(\omega t)\right) \tag{4}$$

Substituting relation (4) into Equation (2), without loss of generality, we may assume that,

$$\frac{\partial \psi}{\partial (p/E)}\phi_1(x)p_1(t)=A\left(\frac{2\pi}{\lambda}\right)^2\cos\left(\frac{2\pi x}{\lambda}\right)\cos(\omega t), \tag{5a}$$

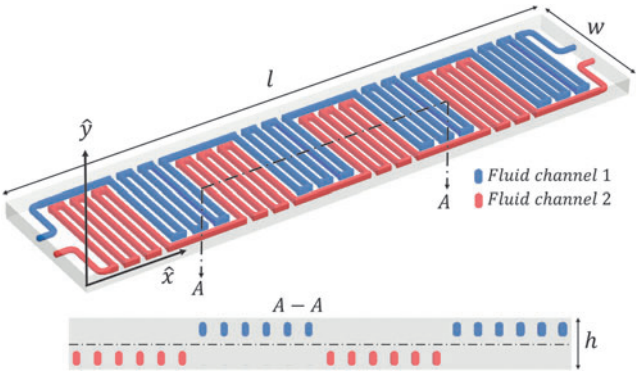

FIG. 1. Illustration of an elastic structure with two sets of embedded fluid-filled channel network (*top*) and its side view (*bottom*). In this specific illustrated case, Channel network 1 is always above neutral surface expressed by positive $\phi_1(x)$ values, and Channel network 2 is always below neutral surface represented by negative $\phi_2(x)$ values. Color images are available online.

$$\frac{\partial\psi}{\partial(p/E)}\phi_2(x)p_2(t) = A\left(\frac{2\pi}{\lambda}\right)^2 \sin\left(\frac{2\pi x}{\lambda}\right)\sin(\omega t). \quad (5b)$$

For the inlet pressures

$$p_1(t) = p_0\cos(\omega t) \quad , \quad p_2(t) = p_0\sin(\omega t) \quad (6)$$

the required channel densities are obtained as

$$\begin{aligned}\phi_1(x) &= \phi_0\cos(2\pi x/\lambda)\\ \phi_2(x) &= \phi_0\sin(2\pi x/\lambda)\end{aligned} \quad (7)$$

and $p_0 = A\kappa^2/(\phi_0\partial\psi/\partial(p/E))$, where $\kappa = 2\pi/\lambda$ is the wave number.

Positive values of channel density function $\phi(x)$ denote channels that are located above the beam's neutral surface, where negative values are located below it (Fig. 1). Equation (7) represents a continuous channel distribution function and needs to be translated to discrete locations. The center of the kth channel, x_k, is calculated by[43]

$$\int_0^{x_k} |\phi(x)|\,dx = k - \frac{1}{2}, \quad (8)$$

where k is a natural number. Figure 2 describes the theoretical channel density function and the inlet pressure of two channels. It also illustrates the locations of the discrete channels, which are located above the neutral surface when the corresponding density function, $\phi_1(x)$ or $\phi_2(x)$, is positive and are located below the neutral surface if $\phi_1(x)$ or $\phi_2(x)$ is negative.

This simple design comprises only two sets of channels and is fabricated easily due to its initial planar shape. We notice that the inlet pressures $p_1(t) = p_0\cos(\omega t)$, $p_2(t) = p_0\sin(\omega t)$ dictate negative gauge pressures, which are limited in magnitude and, in turn, cause a limited deformation. Note that working with liquids in a negative pressure range may initiate phase change. Furthermore, we assume a linear relation between the pressure, p, and the slope change angle, ψ, namely that $\partial\psi/\partial(p/E)$ is constant. Experimentally, this assumption is valid for a certain range of positive gauge pressures but is not satisfied by negative values (see in Supplementary Fig. S1). Thus, for certain cases, it might be beneficial to avoid negative gauge pressures.

To obtain non-negative inlet pressures, we may modify them as follows,

$$\begin{aligned}p_1(t) &= p_0(\cos(\omega t) + 1)\\ p_2(t) &= p_0(\sin(\omega t) + 1)\end{aligned} \quad (9)$$

However, the additional terms multiplied by the channel density function, according to Equation (2), form an undesired curvature invariant with respect to time. To overcome this problem, we may use a third auxiliary channel which is needed to cancel these terms with constant pressure p_3, where the channel density $\phi_3(x)$ may be expressed as,

$$\frac{\partial\psi}{\partial(p/E)}\phi_3(x)p_3 = -A\left(\frac{2\pi}{\lambda}\right)^2\left[\sin\left(\frac{2\pi x}{\lambda}\right) + \cos\left(\frac{2\pi x}{\lambda}\right)\right]. \quad (10)$$

This approach enables to change the wave amplitude of the beam only by adjusting the unbounded applied inlet pressure of all three channels. However, multiple channels increase the possibility of the intersection of the channels' cross-sections, which increases the fabrication complexity and reduces the beam's homogeneity. Hence, to avoid an additional third channel, as well as the third controlled inlet, we may design the beam in a precurved shape instead of the auxiliary channel's constant deformation contribution (Fig. 3). A drawback of this approach is the predetermined amplitude without the ability to tune it as before. From Equations (2) and (10), we calculate the required shape of the precurved beam, $y_0(x)$, as follows

$$y_0(x) = -\sqrt{2}A\sin\left(\frac{2\pi x}{\lambda} + \frac{\pi}{4}\right). \quad (11)$$

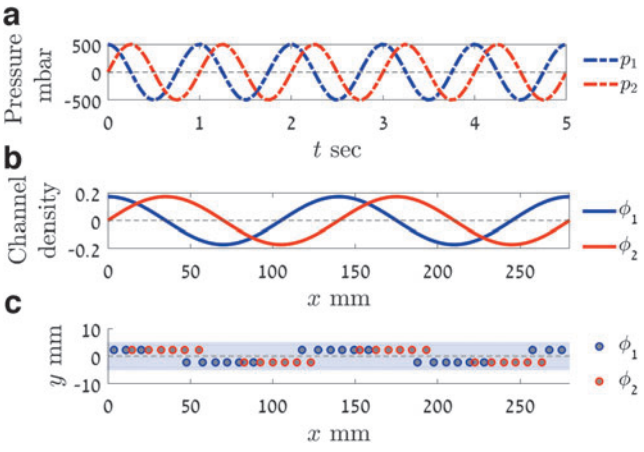

FIG. 2. Theoretical straight robot configuration. **(a)** Inlet pressures of channels 1 and 2 are marked by *dashed blue* and *red lines*, respectively. **(b)** Channel densities of sets 1 and 2 are marked by *blue* and *red lines*, respectively. **(c)** Robot's side view presents initial straight shape and channel locations. Positive values of channel density function $\phi_i(x)$ denote channels that are located above the neutral surface, whereas negative values are located below it. Color images are available online.

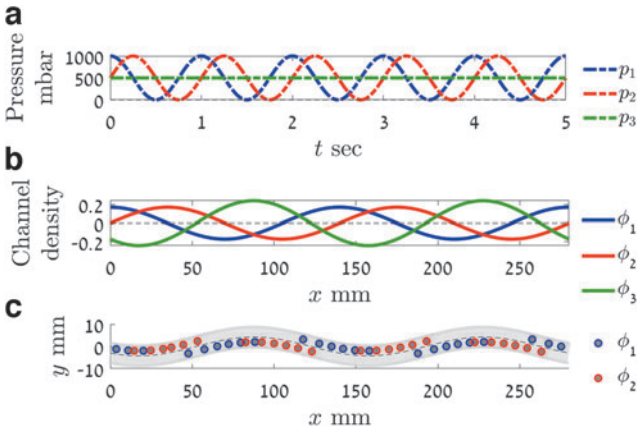

FIG. 3. Theoretical precurved robot configuration. **(a)** Inlet pressures of channels 1, 2, and auxiliary channel 3 are marked by *dashed blue*, *red*, and *green* lines, respectively. **(b)** Channel densities of sets 1, 2 and auxiliary channel 3 are marked by *blue*, *red*, and *green* lines, respectively. **(c)** Robot's side view presents precurved shape y_0 and channel locations. Positive values of channel density function $\phi_i(x)$ denote channels located above the neutral surface, whereas negative values mean location below it. Color images are available online.

Fabrication and Experimental Setup

Fabrication considerations and methods

In the previous section, Equation (7) presents a continuous channel distribution function and its mapping into its discrete locations using Equation (8). Subject to channel distributions, the number of discrete channels, and cross-section geometry, two channels may overlap. In addition, the varying signs of $\phi_1(x)$ and $\phi_2(x)$ place the channels both above and below the neutral surface, which increases fabrication complexity and yields a thicker robot.

According to theoretical model guidelines, we placed the channels with the constraints of nonintersections and a minimal gap of 1 channel diameter between the channels. For each x coordinate, only one channel is located. Limited-strain layers are attached to the top and bottom surfaces, alternately determining the neutral surface and curvature direction. Limited-strain layers replace the need to locate the channels in the distance from the center of structures' cross-section, thus allowing the channels to lie on the center. We found that minor changes in channel locations and the use of limited-strain layers yield a thinner structure and simplify fabrication with little effect on traveling wave motion relative to discrete theoretical design.

In addition, for crawling locomotion, as demonstrated below (Fig. 8), we desire to ensure at least two contact points with the ground during the motion. The minimal wavelength periods to fulfill this requirement is two, that is, $2\lambda \leq l$. Although more wavelength periods increase the robot's speed [see Equation (21) in the Kinematic Analysis section], we chose $\lambda = l/2$, which fulfilled the requirement and was easier to fabricate. The design is illustrated in Figure 4 both for initially straight and precurved robots. The soft robot fabrication process is presented in Figure 5 and detailed in Supplementary Information.

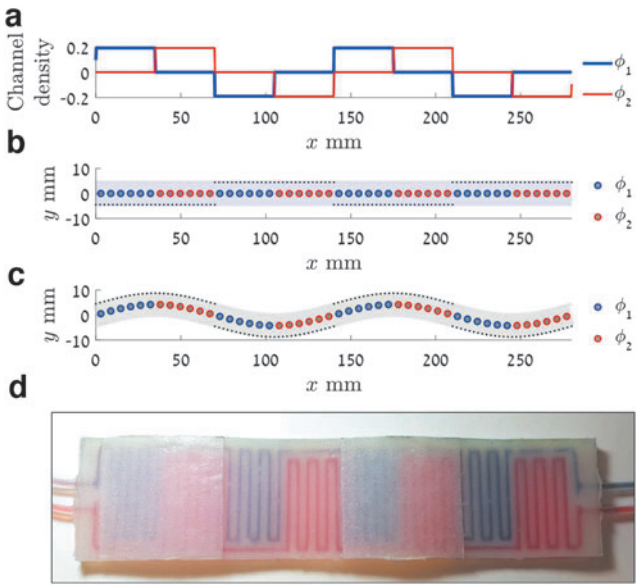

FIG. 4. Robots' design. **(a)** Channel density functions $\phi_1(x)$ and $\phi_2(x)$. **(b)** Straight robot discrete channel locations with added limited-strain layers marked by *dashed lines*. **(c)** Precurved robot discrete channel locations with added limited-strain layers marked by *dashed lines*. The length of the limited-strain layers is described by Equation (24; See Supplementary Information). **(d)** Robot's *top*-view displays two sets of channels and *top* surfaces' limited-strain layers. Color images are available online.

Experimental setup

The robot was placed on a flat surface, and a pressure controller (Elveflow OB1) was connected to its inlets. A camera (Logitech C920, HD, 30fps) was placed perpendicular to the deflection plane and captured frames simultaneously to actuation. To extract deformation signal, we used MATLAB® image processing toolbox to adjust frames before region classification. Utilizing high contrast between the robot's and background color, we were able to apply a simple algorithm on the bimodal histogram to determine threshold value and to extract the robot's shape in time $y(x,t)$. The experimental setup is illustrated in Figure 5g.

Experimental Results

This section presents the experimental results of wave propagation in two types of robots: (i) Initially straight robot (Fig. 4b) having two pressure inlets, varying from negative to positive gauge pressure, in the range from −675 to 530 mbar. (ii) Precurved robot (Fig. 4c) having two inlets subject to positive gauge pressure exclusively, from 300 to 1200 mbar. First, we present the method of measurements, data analysis, and identification to quantify the wave propagation. We display a traveling wave ratio (TWR) map for various inlet pressures for both robots, indicating the preferable inlets to create traveling wave motion.

Experimental identification

We now briefly review an approach to fit a curve to measured data using tempo-spatial decomposition to quantify the propagation wave's quality. This method is well established in References[26,44–46] and extensively detailed in Supplementary Information. The outcome of the process may help tuning the real system's controlled inlets to achieve an effective traveling wave.

Once the deformation measurements $y(x,t)$ have been extracted from images, the deformation signal can be decomposed in time and space[26] and takes the form of a truncated Fourier series which describes the wave as a sum of several one-dimensional (1D) waves that have different frequencies and wavelengths. The first harmonic associated with the robot's designed wave number and the excitation frequency has greater amplitude, in order of magnitude, than the other modes. While it is possible to analyze each one of the decomposed 1D waves, all other modes have minor contribution to the propagation. Hence, we are interested only in the first harmonic which is further analyzed.

The first harmonic, composed of a single frequency and wavelength, can be written as a combination of two traveling waves propagating in opposite directions,

$$y(x,t) = \Re\left(U_+ e^{i(\omega t - \kappa x)} + U_- e^{i(\omega t + \kappa x)}\right), \qquad (12)$$

where U_+ and U_- are the complexes forward and backward wave's amplitudes, respectively, which can be obtained from the tempo-spatial decomposition (Supplementary Information) and determine the behavior of a single wave, including its magnitude and direction.

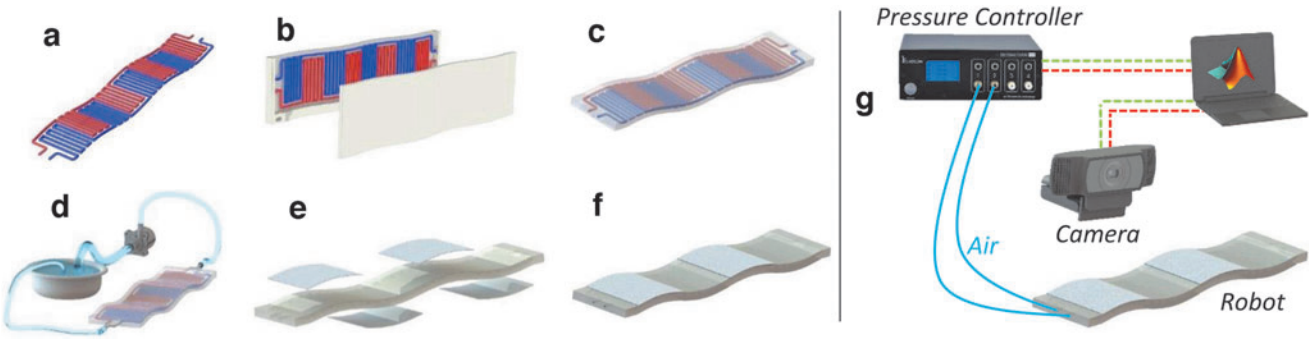

FIG. 5. Fabrication process and experimental setup. **(a)** 3D printed PVA channels' cores. **(b)** PLA mold for silicone casting around a channel's core. **(c)** Elastic structure with embedded PVA core. **(d)** PVA core dissolving process using circulating water pump. **(e)** Limited-strain layers glued to surfaces. **(f)** Fabricated robot. **(g)** Experimental setup includes simultaneous trigger on Pressure controller, which is connected to two robot's inlets and frame grab using HD camera. PLA, polylactic acid; PVA, polyvinyl alcohol. Color images are available online.

The TWR is a scalar parameter that quantifies single wave propagation characteristics which is possible due to the modal decomposition. We can define the TWR as the ratio between the standing wave and the mixed-wave amplitude,[44,46]

$$TWR = 1 - \frac{||U_+| - |U_-||}{|U_+| + |U_-|}. \tag{13}$$

This bounded ratio, $0 \leq TWR \leq 1$, defines the propagation of a wave, where $TWR = 0$ denotes pure traveling wave, whereas $TWR = 1$ denotes pure standing wave. Any other value between 0 and 1 expresses a mixed traveling and standing wave. Moreover, the wave's direction can be obtained by the sign of $|U_+| - |U_-|$, positive or negative, which corresponds to forward or backward direction, respectively.

The described identification procedure gives rise to map the propagation behavior of the robot for each set of inputs and helps tuning the input parameters to create traveling wave.

Straight robot with two inlets of negative to positive gauge pressure range

A straight beam shape design consists of two sets of channels with time phase inputs and spatial phase distribution as presented above. The gradient $\gamma^+ \triangleq \partial\psi/\partial(p/E)^+$ is nearly constant for a certain positive range of pressure. For the negative gauge pressure range, the gradient is also approximately constant. However, it has a moderately smaller slope where $\gamma^+ \approx 1.27\gamma^-$ as shown in Supplementary Figure S1a. To create the same deformation amplitudes for both positive and negative gauge pressure inlets, we need to compensate for the lower slope by applying larger absolute pressure as shown in Supplementary Figure S1b satisfying $p_0^- \gamma^+ = p_0^+ \gamma^-$. Thus, inlet pressures are calculated by

$$\begin{aligned} p_1(t) &= \min\left[p_0^+ \cos(\omega t), p_0^- \cos(\omega t)\right], \\ p_2(t) &= \min\left[p_0^+ \sin(\omega t), p_0^- \sin(\omega t)\right]. \end{aligned} \tag{14}$$

Once controlled inlets for negative gauge pressure are calibrated, we denote by $\hat{p}_i$ the nominal inlet pressure where $\hat{p}_i = p_0^+$ and $i = 1, 2$ is the inlet number. Generally, two sinusoidal inlets have three controlled parameters: $\hat{p}_1, \hat{p}_2$, and phase shift θ, given by

$$p_1(t) = \hat{p}_1 \sin(\omega t + \theta) \quad , \quad p_2(t) = \hat{p}_2 \sin(\omega t). \tag{15}$$

Aiming to create a pure traveling wave pattern, we may set $\hat{p}_1 = \hat{p}_2$ and phase shift of $\theta = \pi/2$ which essentially yields Equation (6). However, dealing with an actual system, we expect inaccuracies caused by fabrication methods, design compromises, and unmodeled phenomena. Hence, tuning the three controlled inlets $\hat{p}_1, \hat{p}_2$, and θ may improve the quality of the traveling wave.

To tune the controlled parameters, they were tested experimentally at the ranges between $\hat{p}_1, \hat{p}_2 = 300$ and 530 mbar with 11 equally spaced values and phase shift θ from 0 to π with 11 equally spaced values. The measured tempo-spatial deformation under each inlet set was analyzed and quantified using TWR value, as explained in the previous section.

Figure 6a illustrates the robot's traveling wave pattern in space and time at $\hat{p}_1, \hat{p}_2 = 530$ and $\theta = \pi/2$. Figure 6b presents TWR map as function of controlled parameters where, for brevity, a smooth two-dimensional (2D) surface was generated from 11×11 grid points at $\theta = \pi/2$ using *contourf* command in MATLAB. Theoretically, we expect to get minimum values of TWR, that is, best traveling waves, along the principal diagonal line where $\hat{p}_1 = \hat{p}_2$ according to Equation (6). Along the diagonal, waves are close to pure traveling waves, and their amplitudes increase as $\hat{p}_1$ and $\hat{p}_2$ become larger. We can observe the expected diagonal yet with a slight deviation from the exact symmetry line $\hat{p}_1 = \hat{p}_2$. This deviation is associated with model inaccuracies and small asymmetries in the structure and two-channel sets.

Precurved robot having two inlets subject to positive gauge pressure

Using only positive gauge pressure simplifies actuation, avoids cavitation issues, and also can create larger amplitudes. Based on the previous theoretical section, we created a precurved elastic robot, where its initial shape is according to Equation (11) with wavelength of $\lambda = l/2$ and amplitude of $A \approx 2$ mm. Figure 4 illustrates its design.

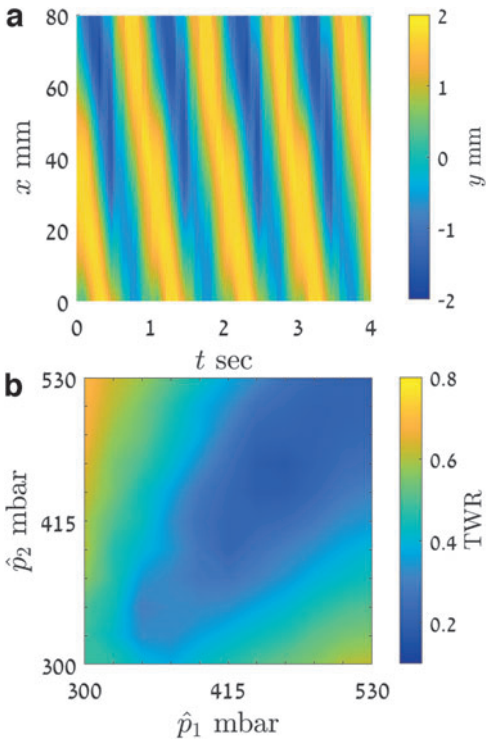

FIG. 6. Experimental results of measurements and data analysis for the straight robot. **(a)** A typical image of wave propagation. *Color* map represents measured deflection, $y(x,t)$, demonstrating traveling wave pattern in space and time for $\hat{p}_1 = 530$ mbar, $\hat{p}_2 = 530$ mbar, and $\theta = \pi/2$. **(b)** *Color* map represents low (cool) and high (warm) values of TWR for different values of $\hat{p}_i$ introduced at channels $i = 1, 2$ and phase shift of $\theta = \pi/2$. Low TWR values which are located approximately along the principal diagonal (theoretical diagonal at $\hat{p}_1 = \hat{p}_2$) represent propagating waves. Tick marks on axes denote the 11×11 grid of values for which the measurements were undertaken. TWR, traveling wave ratio. Color images are available online.

Similar to the previous section, Equation (7) still represents the channels' densities along the x coordinate, and the same considerations regarding the practical fabrication of embedded channel network are valid. Equation (9) represents the applied inlet pressure of each channel in the case of exclusively positive gauge pressure, and in this case, $\gamma = \partial\psi/\partial(p/E)$ is nearly constant for the whole range of motion.

As previously, we aim to tune the three controlled parameters $\hat{p}_1, \hat{p}_2$, and θ, to achieve pure traveling wave motion as close as possible. The inlets are given by,

$$\begin{aligned} p_1(t) &= \hat{p}_1(\sin(\omega t + \theta) + 1) \\ p_2(t) &= \hat{p}_2(\sin(\omega t) + 1). \end{aligned} \tag{16}$$

Due to the symmetry, theoretically we may set $\hat{p}_1 = \hat{p}_2$ and phase shift of $\theta = \pi/2$, which yield the pure traveling wave inlets as stated in Equation (9). However, due to the mentioned inaccuracies, we wish to tune the parameters. We experimentally tested the robot with 11 equally spaced values of the pressure at the inlets in the range from $\hat{p}_1, \hat{p}_2 = 300$ to 600 mbar and 11 equally spaced values of the phase shift, θ, in the range from 0 to π. Each experiment was analyzed, and the TWR of each wave was obtained.

Figure 7a illustrates the propagating wave in space and time at $\hat{p}_1 = 540$ mbar, $\hat{p}_2 = 480$ mbar, and $\theta = \pi/2$. Figure 7b presents TWR map as a function of controlled parameters where, for brevity, smooth 2D surface was generated from 11×11 grid points at $\theta = \pi/2$ using *contourf* command in MATLAB. The area in which the lowest value of TWR (cold colors) is displayed is located approximately along the principal diagonal line where $\hat{p}_1 = \hat{p}_2$. Unlike the case of the straight robot, now the ideal wave's amplitude is predetermined and cannot be altered. Thus, ideal performance is expected at $\hat{p}_1 = \hat{p}_2 = A\kappa^2/(\phi_0\gamma)$. Due to the mentioned inaccuracies, the experimental working point, marked by "+" on the TWR map approximately at $\hat{p}_1 = 540$ mbar, $\hat{p}_2 = 480$ mbar, is not positioned exactly on $\hat{p}_1 = \hat{p}_2$ line. Any applied pressures lower than the working point pressures will be insufficient to equalize the amplitude opposite to the precurved shape.

Similarly, applied pressures greater than the working point increase the amplitude of the opposite side beyond the precurved robot designed amplitude. In these cases, propagating modes, if there are any, will not oscillate around the desired $y = 0$ axis but around a deviation function $d(x) \approx D\sin(\kappa x + \vartheta)$. The ideal (desired) case is $D \approx 0$, where the robot oscillates about $y = 0$, that is, the inlet pressures are roughly equal to working point pressures. In the case where inlet pressures are zeroed, $d(x)$ takes the form of the initially curved robot. Figure 7c presents the color map of the deviation amplitude D for varying $\hat{p}_1, \hat{p}_2$. The experimental working point is marked by "+" representing the working point at $\hat{p}_1 = 540$ mbar, $\hat{p}_2 = 480$ mbar where the deviation gets its lowest value, $D \approx 0$.

Previous TWR maps (Figs. 6 and 7a–c) were calculated for various ranges of $\hat{p}_1, \hat{p}_2$ at the fixed phase shift of $\theta = \pi/2$, as stated theoretically in pressure inlets' Equations (6) and (9). Figure 7d, which exhibits experimentally the influence of the temporal phase shift θ on the TWR, displays a minimum value of TWR at approximately $\theta = \pi/2$ for fixed values of $\hat{p}_1 = 540$ mbar and $\hat{p}_2 = 480$ mbar. An analytic expression for TWR as a function of θ for 1D wave may be expressed as,

$$TWR(\theta) = 1 - \frac{\left|\sqrt{1+\sin\theta} - \sqrt{1-\sin\theta}\right|}{\sqrt{1+\sin\theta} + \sqrt{1-\sin\theta}}. \tag{17}$$

This analytic expression is overlaid in Figure 7d by a dashed line, showing a very good agreement with the experimentally measured value.

Traveling-Wave Robot Locomotion

This section presents the underlying kinematics of locomotion of the traveling wave soft robots on the ground and shows the experimental demonstration of soft robots in several scenarios.

Kinematic analysis

Assuming that the robot's neutral surface generates a general 1D wave motion, which may be expressed as

$$y(x,t) = A(\cos(\kappa x)\sin(\omega t + \theta) + \sin(\kappa x)\sin(\omega t)), \tag{18}$$

let us consider a fixed material point located at the lower boundary surface of the beam, which comes in contact with

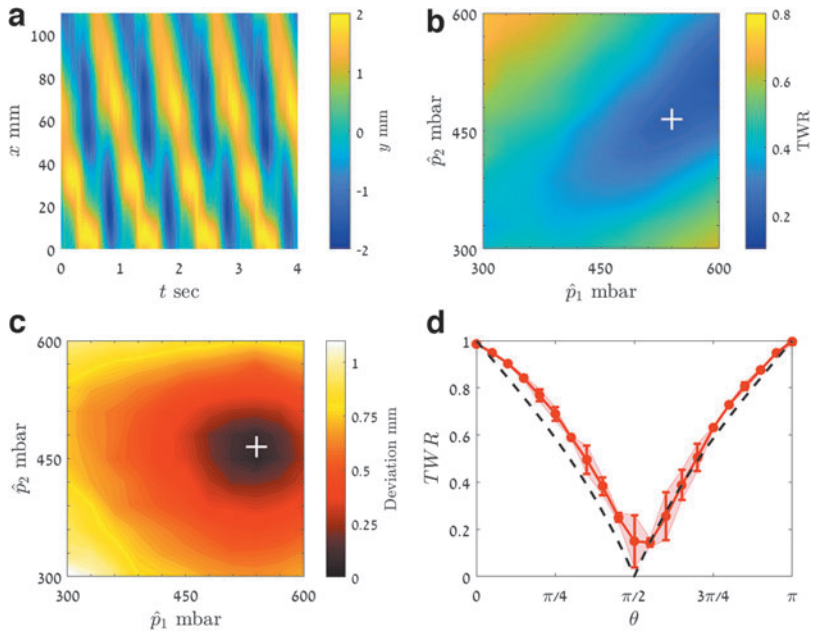

FIG. 7. Experimental results of measurements and data analysis for the precurved robot. **(a)** A typical image of wave propagation. Color map represents measured deflection, $y(x,t)$, demonstrating propagating wave pattern in space and time for $\hat{p}_1 = 540$ mbar, $\hat{p}_2 = 480$ mbar, and $\theta = \pi/2$. **(b)** TWR map for different values of $\hat{p}_i$ introduced at channels $i = 1, 2$. Color map represents low (cool) and high (warm) values of TWR. Low TWR values are located approximately along the principal diagonal line. Working point is marked by "+". **(c)** Lowest deviation amplitude from the desired wave is nearly zero at the working point pressure, marked by "+". Tick marks on axes denote the 11×11 grid of values for which the measurements were undertaken. **(d)** The effect of temporal phase shift, θ, on the measured TWR in a precurved robot for $\hat{p}_1 = 540$ mbar and $\hat{p}_1 = 480$ mbar, is marked by *red* dots. Measured TWR function versus θ attains minimum at approximately $\theta = \pi/2$. The corresponding analytic curve of TWR as a function of θ is marked by a dashed *black* line. Color images are available online.

the floor. The point under consideration shares the same cross-sectional plane with a material point located at x on the neutral surface. Thus their relative displacement is always perpendicular to the backbone curve $y(x,t)$ whose tangent is oriented by angle $\varphi(x,t) = \tan^{-1}(\partial y/\partial x)$, as shown in Figure 8. In the robot's coordinate frame, $\hat{\mathbf{x}}' - \hat{\mathbf{y}}'$, we can describe the point's position as

$$\mathbf{r}'_b(x,t) = \left[x + \frac{h}{2}\sin\varphi\right]\hat{\mathbf{x}}' + \left[y(x,t) - \frac{h}{2}\cos\varphi\right]\hat{\mathbf{y}}'. \quad (19)$$

In the general case, the robot alternates its contact points with the ground. Assuming kinematic constraint of no-slip contact, the absolute velocity of the instantaneous contact point, in $\hat{\mathbf{x}}'$ direction, is zero. Thus, the robot's velocity $v_f(t)$ in $\hat{\mathbf{x}}'$ direction is equal in magnitude and opposite in direction to the contact point's instantaneous velocity $v_c^x(t)$, with respect to $\hat{\mathbf{x}}' - \hat{\mathbf{y}}'$ coordinate frame, so that $v_f(t) = -v_c^x(t)$.[47] It is emphasized that friction forces are essential for creating propulsion and depend on the normal contact force related to gravitational load. The expression for the robot's instantaneous velocity is given by

$$v_f(t) = \frac{Ah\kappa\omega \ \sin(\theta)}{2\sqrt{\sin^2(\omega t) + \sin^2(\omega t + \theta)}}. \quad (20)$$

For the special case, where $\theta = \pi/2$, that is, pure traveling wave, by assuming that $A^2\kappa^2 = 1$, Equation (19) gives an approximate point's position which moves along the trajectory of an ellipse in $\hat{\mathbf{x}}' - \hat{\mathbf{y}}'$ plane with semimajor axis $a = A$ and semiminor axis $b = A\kappa\frac{h}{2}$ (Fig. 8). The velocity in this case becomes constant, where $v_f(t) = v_f = Ah\kappa\omega/2$. Another two special cases are when $\theta = \{0, \pi\}$, meaning pure standing wave, in which case the velocity of the robot vanishes.

To characterize the robot's speed, let us define the Advance Ratio,[47] which is the robot's speed relative to the wave speed

$$AR \triangleq \frac{v_f}{v_{wave}} = \frac{\pi^2}{2}\frac{A}{\lambda}\frac{h}{\lambda} \quad (21)$$

where A/λ and h/λ are the ratios of the robot's amplitude and thickness to the wavelength, respectively. It is now convenient to see that the advance ratio is proportional to the ratios of A/λ and h/λ, which depend on the geometrical properties that can be tuned during the design process.

Next, we study the effect of the phase shift θ on the net propagation speed. For an arbitrary phase shift θ the robot's velocity $v_f(t)$ oscillates and is not constant, as stated in Equation (20). The average velocity of the robot is given by,

$$\bar{v}_f = \frac{1}{T}\int_0^T v_f(t)\,dt. \quad (22)$$

where $T = 1/f$ is the time cycle. Figure 8b examines the effect of the temporal phase shift on the robot's velocity for a fixed $\hat{p}_1 \approx \hat{p}_2$, under the assumptions of quasi-static motion and no-slip kinematic constraint, visualizing that the maximal velocity is attained for $\theta \approx \pi/2$, where the deformation

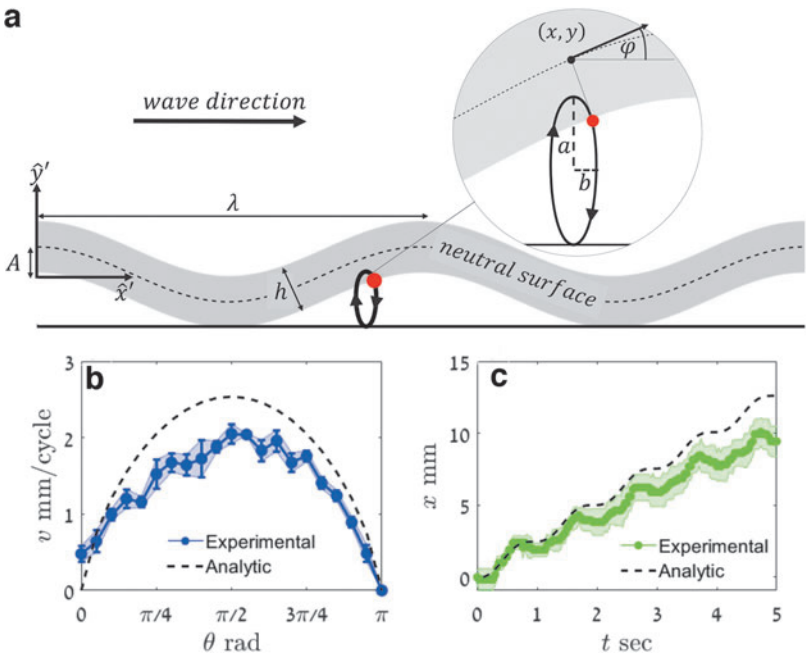

FIG. 8. **(a)** Traveling wave robot locomotion illustration. The neutral surface oscillates as an one-dimensional wave, where A is the wave amplitude, λ is the wavelength, and h is robot's height. A path of the material point on a surface contacting the ground is illustrated for the case where $\theta = \pi/2$, which creates an approximate ellipse in $\hat{\mathbf{x}}' - \hat{\mathbf{y}}'$ plane, where semimajor and semiminor axes are $a = A$ and $b = A\kappa h/2$, respectively. **(b)** The effect of the temporal phase shift on the robot's velocity for a fixed $\hat{p}_1 \approx \hat{p}_2$. **(c)** The trace of a point located at a distance of $h/2$ from the neutral surface along 5 cycles. Color images are available online.

pattern is closest to pure traveling wave as it was seen above, in Figure 7d. Moreover, the velocity is approximately zero when $\theta = \{0, \pi\}$, which corresponds to a standing wave. An analytic result which was obtained in Equation (22) is overlaid in Figure 8b, showing a good agreement.

For the special case, where $\theta = \pi/2$, that is, pure traveling wave, Figure 8c depicts the trace of a point located at a distance of $h/2$ from the neutral surface, both experimentally and analytically according to

$$\mathbf{r}_b(x,t) \cdot \hat{\mathbf{x}} = \frac{1}{2} Ah\kappa\omega t + \frac{A\kappa h \sin(\omega t - \kappa x)}{2\sqrt{1 + A^2\kappa^2 \sin^2(\omega t - \kappa x)}}. \quad (23)$$

Demonstrations

Visualization of the traveling wave motion is illustrated by the straight robot in Figure 9a, where several snapshots were taken during one time cycle at $t = 0, T/4, T/2, 3T/4, T$, where one can observe that the peak is advancing from left to right. Figure 9b illustrates precurved robot's propagation on a horizontal surface, with an average velocity of $v_f \approx 2.2$ mm/cycle.

Several additional scenarios were tested to demonstrate the robot's locomotion capabilities. When one end is held fixed, the robot can act as a conveyor to transport objects in the direction opposing the wave's propagation. Such configuration is illustrated in Figure 9c, where the oscillating precurved robot is attached at the right end and its wave direction is from right to left. The robot is conveying a small block with the sign of the Technion logo in the opposite direction to the wave, that is, from left to right. An additional capability of traveling wave soft robots is to exploit their flexibility to move through narrow spaces. Soft robot climbing vertically (Fig. 9d) and crawling horizontally (Fig. 9e, f) in a narrow gap between two parallel plates is demonstrated. In addition, the traveling wave soft robots' flexibility and compliance can also be utilized for crawling in a pipe, as shown in Figure 9g. A Supplementary Movie S1 includes illustrations of the described scenarios.

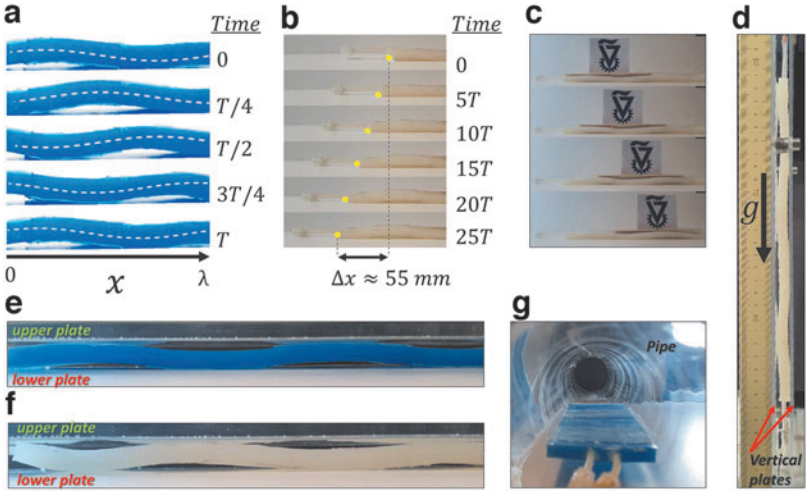

FIG. 9. Robots' snapshots during motion. **(a)** Robot's shape during one time cycle T, illustrated by the straight robot. Analytic wave shape is marked by dashed *white* line. **(b)** Precurved robot propagation during 25 time cycles which moves 55 mm with an average velocity of $v_f \approx 2.2$ mm/cycle. **(c)** The precurved robot is held at the *right* end, acting as a conveyor carrying a small block with the sign of the Technion logo in the opposite direction to the wave. **(d)** Precurved robot is climbing vertically between two plates. **(e)** Straight and **(f)** precurved robots propagating between two plates. **(g)** Straight robot crawling through a tube. Color images are available online.

Conclusion

The formation of traveling waves in slender elastic configurations is of applicative importance and may pave the way to progress in many fields that utilize propulsion in unpredictable and narrow passages such as disaster areas or within vascular systems. Moving waves allow for thrust to be applied throughout the robot, thus to self-propel in a long and winding path.

In this work, we present a model-based method to design and generate continuous traveling waves in elastic structures with a fluidic network using only two controlled pressure inlets. This reduction in inlets simplifies the implementation in confined spaces and on-board platforms due to fewer hardware components and overall weight. First, we provided theoretical analysis that guided the design of the channel network distribution and the corresponding continuous pressure inlets. Then, using standard and simple casting techniques, we fabricated two types of soft robots capable of generating bidirectional traveling waves. Next, we conducted experiments, analyzed the generated waves, and applied a method of inlet calibration. Finally, we provided a kinematic analysis that allows gait planning and demonstrated robot locomotion in various scenarios.

The experimental results agree well with the simplified theoretical models. However, deviations of experimental values from the theoretical model are associated with design compromises, fabrication inaccuracies, and unmodeled effects such as inertia, external forces, contacts, and nonlinearity of the elastic structure that future works may address. In particular, advanced fabrication techniques, such as multimaterial 3D printers, may offer new design possibilities to create such composite structures. It may offer better fabrication resolution, various materials, and new channel network geometries to implement the theoretical model more accurately.

A possible improvement of locomotion performance is avoiding slippage to the opposite direction of the wave's direction. This is one of the causes of slight speed mitigation between experimental speed values and theoretical ones. Taking measures such as attaching a high-friction material, coarse skin, or asymmetric friction using scale-like skin may help avoiding slippage. In addition, optimization of locomotion performance may be included in future works. Finally, the presented robot is not restricted to crawling locomotion but may also be applied for swimming. One may fill the channels with water and utilize a similar density of silicone and water to obtain neutral buoyancy between the robot and surrounding liquid. Generating traveling waves in the elastic body will create thrust.

Authors' Contributions

All authors contributed to the design and implementation of the research, to the analysis of the results, and to the writing of the article.

Author Disclosure Statement

No competing financial interests exist.

Funding Information

This research has been supported by Israeli Science Foundation (ISF) under grant no. 1005/19, and by the Israeli Ministry of Science and Technology under grant no. 3-15622.

Supplementary Material

Supplementary Information
Supplementary Figure S1
Supplementary Movie S1

References

1. Trivedi D, Rahn CD, Kier WM, *et al.* Soft robotics: biological inspiration, state of the art, and future research. Appl Bionics Biomech 2008;5:99–117.
2. Kim S, Laschi C, Trimmer B. Soft robotics: a bioinspired evolution in robotics. Trends Biotechnol 2013;31:287–294.
3. Polygerinos P, Correll N, Morin SA, *et al.* Soft robotics: review of fluidâĂŘdriven intrinsically soft devices; manufacturing, sensing, control, and applications in humanâĂŘrobot interaction. Adv Eng Mater 2017;19:1700016.
4. Shepherd RF, Ilievski F, Choi W, *et al.* Multigait soft robot. Proc Natl Acad Sci U S A 2011;108:20400–20403.
5. Tolley MT, Shepherd RF, Mosadegh B, *et al.* A resilient, untethered soft robot. Soft Robot 2014;1:213–223.
6. Umedachi T, Vikas V, Trimmer BA. Highly deformable 3-d printed soft robot generating inching and crawling locomotions with variable friction legs. In: 2013 IEEE/RSJ International Conference on Intelligent Robots and Systems. Tokyo, Japan: IEEE, 2013:4590–4595.
7. Mao S, Dong E, Jin H, *et al.* Gait study and pattern generation of a starfish-like soft robot with flexible rays actuated by SMAs. J Bionic Eng 2014;11:400–411.
8. Kamamichi N, Yamakita M, Asaka K, *et al.* A snake-like swimming robot using IPMC actuator/sensor. In: Proceedings 2006 IEEE International Conference on Robotics and Automation, 2006. ICRA 2006. Orlando, FL: IEEE, 2006: pp. 1812–1817.
9. Boxerbaum AS, Shaw KM, Chiel HJ, *et al.* Continuous wave peristaltic motion in a robot. Int J Robot Res 2012;31:302–318.
10. Rafsanjani A, Zhang Y, Liu B, *et al.* Kirigami skins make a simple soft actuator crawl. Sci Robot 2018;3:eaar7555.
11. Onal CD, Chen X, Whitesides GM, *et al.* Soft mobile robots with on-board chemical pressure generation. In: Robotics Research. Cham: Springer, 2017:525–540.
12. Lin H.-T, Leisk GG, Trimmer B. Goqbot: a caterpillar-inspired soft-bodied rolling robot. Bioinspiration Biomimetics 2011;6:026007.
13. Feng H, Sun Y, Todd PA, *et al.* Body wave generation for anguilliform locomotion using a fiber-reinforced soft fluidic elastomer actuator array toward the development of the eel-inspired underwater soft robot. Soft Robot 2020;7:233–250.
14. Gao L, Qin H, Li P. Hydrodynamic analysis of fishâĂŹs traveling wave based on grid deformation technique. Int J Offshore Polar Eng 2021;31:178–185.
15. Marchese AD, Onal CD, Rus D. Autonomous soft robotic fish capable of escape maneuvers using fluidic elastomer actuators. Soft Robot 2014;1:75–87.
16. Morawski M, Malec M, Szymak P, *et al.* Analysis of parameters of traveling wave impact on the speed of biomimetic underwater vehicle. Solid State Phenom 2014;210:273–279, Trans Tech Publ.
17. Mojarrad M, Shahinpoor M. Biomimetic robotic propulsion using polymeric artificial muscles. Proc Int Conf Robot Autom 1997;3:2152–2157.

18. DobrolyubovA. The mechanism of locomotion of some terrestrial animals by travelling waves of deformation. J Theor Biol 1986;119:457–466.
19. Chirikjian GS, Burdick JW. The kinematics of hyper-redundant robot locomotion. IEEE Trans Robot Autom 1995;11:781–793.
20. Chen L, Wang Y, Ma S, *et al.* Analysis of traveling wave locomotion of snake robot. In: IEEE International Conference on Robotics, Intelligent Systems and Signal Processing, 2003. Proceedings. 2003, Vol. 1. IEEE, 2003: 365–369.
21. Chen L, Ma S, Wang Y, *et al.* Design and modelling of a snake robot in traveling wave locomotion. Mech Mach Theory 2007;42:1632–1642.
22. Stalbaum T, Hwang T, Trabia S, *et al.* Bioinspired travelling wave generation in soft-robotics using ionic polymer-metal composites. Int J Intell Robot Appl2017;1: 167–179.
23. Jafferis NT, Sturm JC. Fundamental and experimental conditions for the realization of traveling-wave-induced aerodynamic propulsive forces by piezoelectrically deformed plastic substrates. J Microelectromech Syst 2013; 22:495–505.
24. Poole AD, Booker JD, Wishart CL, *et al.* Performance of a prototype traveling-wave actuator made from a dielectric elastomer. IEEE/ASME Trans Mechatron 2012;17:525–533.
25. Setter E, Bucher I, Haber S. Low-Reynolds-number swimmer utilizing surface traveling waves: analytical and experimental study. Phys Rev E 2012;85:066304.
26. Setter E, Bucher I, Haber S. Propulsion at low Reynolds numbers by multiple traveling waves. Proc Inst Mech Eng Part C J Mech Eng Sci 2014;228:2938–2949.
27. Suzumori K, Hama T, Kanda T. New pneumatic rubber actuators to assist colonoscope insertion. In: International Conference on Robotics and Automation (ICRA). Orlando, FL: IEEE, 2006:1824–1829.
28. Onal CD, Rus D. Autonomous undulatory serpentine locomotion utilizing body dynamics of a fluidic soft robot. Bioinspiration Biomimetics 2013;8:026003.
29. Luo M, Pan Y, Skorina EH, *et al.* Slithering towards autonomy: a self-contained soft robotic snake platform with integrated curvature sensing. Bioinspiration Biomimetics 2015;10:055001.
30. Branyan C, Fleming C, Remaley J, *et al.* Soft snake robots: Mechanical design and geometric gait implementation. In: 2017 IEEE International Conference on Robotics and Biomimetics (ROBIO). Macau, Macao: IEEE, 2017:282–289.
31. Lin H, Leisk G, Trimmer B. Soft robots in space: a perspective for soft robotics. Acta Futura 2013;6:69–79.
32. Takayama T, Takeshima H, Hori T, *et al.* A twisted bundled tube locomotive device proposed for in-pipe mobile robot. IEEE/ASME Trans Mechatron 2015;20: 2915–2923.
33. Ozaki K, Wakimoto S, Suzumori K, *et al.* Novel design of rubber tube actuator improving mountability and drivability for assisting colonosocope insertion. In: International Conference on Robotics and Automation (ICRA). Shanghai, China: IEEE, 2011:3263–3268.
34. Watanabe M, Tsukagoshi H. Soft sheet actuator generating traveling waves inspired by gastropod's locomotion. In: International Conference on Robotics and Automation (ICRA). Singapore: IEEE, 2017:602–607.
35. Qi X, Shi H, Pinto T, *et al.* A novel pneumatic soft snake robot using traveling-wave locomotion in constrained environments. IEEE Robot Autom Lett 2020;5:1610–1617.
36. Vasios N, Gross AJ, Soifer S, *et al.* Harnessing viscous flow to simplify the actuation of fluidic soft robots. Soft Robot 2020;7:1–9.
37. Futran CC, Ceron S, Mac Murray BC, *et al.* Leveraging fluid resistance in soft robots. In: International Conference on Soft Robotics (RoboSoft). Livorno, Italy: IEEE, 2018: 473–478.
38. Glozman D, Hassidov N, Senesh M, *et al.* A self-propelled inflatable earthworm-like endoscope actuated by single supply line. IEEE Trans Biomed Eng 2010;57:1264–1272.
39. Lim J, Park H, An J, *et al.* One pneumatic line based inchworm-like micro robot for half-inch pipe inspection. Mechatronics 2008;18:315–322.
40. Matia Y, Elimelech T, Gat AD. Leveraging internal viscous flow to extend the capabilities of beam-shaped soft robotic actuators. Soft Robot 2017;4:126–134.
41. Gamus B, Salem L, Ben-Haim E, *et al.* Interaction between inertia, viscousity and elasticisy in soft robotic actuator with fluidic network. IEEE Trans Robot 2018 2017;34:81.
42. Salem L, Gamus B, Or Y, *et al.* Leveraging viscous peeling to create and activate soft actuators and microfluidic devices. Soft Robot 2020;7:76–84.
43. Matia Y, Gat AD. Dynamics of elastic beams with embedded fluid-filled parallel-channel networks. Soft Robot 2015;2:42–47.
44. Vered Y, Bucher I. Experimental multimode traveling waves identification in an acoustic waveguide. Mech Syst Sig Process 2021;153107515.
45. Bucher I, Gabai R, Plat H, *et al.* Experimental travelling waves identification in mechanical structures. Math Mech Solids 2019;24:152–167.
46. Bucher I. Estimating the ratio between travelling and standing vibration waves under non-stationary conditions. J Sound Vib 2004;270:341–359.
47. Zarrouk D, Mann M, Degani N, *et al.* Single actuator wave-like robot (saw): design, modeling, and experiments Bioinspiration Biomimetics 2016;11:046004.

Address correspondence to:
Lior Salem
Faculty of Mechanical Engineering
TSAP - Technion Autonomous Systems and Robotics Program
Technion - Israel Institute of Technology
Technion City 3200003
Israel

E-mail: liorsal@campus.technion.ac.il